PHYSICS OF FLUIDS **27**, 016603 (2015)

Effects of turbulent eddies and Langmuir circulations on scalar transfer in a sheared wind-driven liquid flow

Naohisa Takagaki,[1] Ryoichi Kurose,[1,a)] Yuta Tsujimoto,[1] Satoru Komori,[1] and Keiko Takahashi[2]

[1]*Department of Mechanical Engineering and Science and Advanced Research Institute of Fluid Science and Engineering, Kyoto University, Kyoto 615-8140, Japan*
[2]*Center for Earth Information Science and Technology (CEIST), Japan Agency for Marine-Earth Science and Technology (JAMSTEC), Yokohama 236-0001, Japan*

(Received 3 August 2014; accepted 30 December 2014; published online 14 January 2015)

The effects of turbulent eddies and Langmuir circulations in liquid flow on scalar transfer across a sheared wind-driven gas-liquid interface are investigated by means of a direct numerical simulation of a gas–liquid two-phase turbulent flow with a wind-driven nonbreaking wavy interface. The wind-driven wavy gas-liquid interface is captured using an arbitrary Lagrangian-Eulerian method with boundary-fitted coordinates on moving grids. The results show that Langmuir circulations are generated on the liquid side below the sheared wind-driven gas-liquid interface. The marker particles on the gas-liquid interface, the turbulent eddies in the form of streamwise vortices on the liquid side (i.e., the typical horseshoe vortices associated with bursting motions), and the low scalar flux lines on the gas-liquid interface induced by the turbulent eddies on the liquid side tend to locally concentrate in the regions along the downward flows caused by the Langmuir circulations. It is suggested that the turbulent eddies on the liquid side mainly control the scalar transfer across the sheared wind-driven gas-liquid interface, and the effect of the Langmuir circulations is relatively small. © *2015 AIP Publishing LLC.* [http://dx.doi.org/10.1063/1.4905845]

I. INTRODUCTION

Heat and mass transfer phenomena across gas-liquid interfaces are encountered in many geophysical and industrial processes, and it is therefore of great importance to clarify such scalar transfer mechanism and model them in order to precisely predict climate and weather and to adequately operate industrial plants. To clarify the scalar transfer mechanism and to evaluate precisely the level of scalar transfer across the wind-driven wavy gas-liquid interface, researchers have conducted field observations (e.g., Wanninkhof and McGillis;[1] McGillis *et al.*;[2] McNeil and D'Asaro[3]), laboratory experiments using a wind-wave tank (e.g., Jähne *et al.*;[4–6] Wanninkhof;[7] Komori *et al.*;[8,9] Iwano *et al.*[10]), and direct numerical simulations (DNSs) of gas-liquid two-phase turbulent flows with wind-driven wavy interfaces (e.g., Kunugi *et al.*;[11] Lakehal *et al.*;[12–14] Banerjee *et al.*;[15] Banerjee;[16] Komori *et al.*[17]). Komori *et al.*[8,9,17] reported that the scalar transfer is enhanced by surface-renewal turbulent eddies in the form of streamwise vortices generated on the liquid side beneath the interfaces. Moreover, Langmuir circulations, which are longitudinal vortices aligned with the wind and considered to be induced by the interaction of Stokes drift and shear (Craik and Leibovich;[18] Leibovich;[19] Thorpe[20]), are also thought to play an important role for scalar transfer across the gas-liquid interface (e.g., McWilliams *et al.*;[21] Sullivan and McWilliams;[22] Garbe *et al.*[23]). Although such Langmuir circulations are often seen in the ocean and lakes, Melville *et al.*[24] found through the laboratory experiments with wind wave tank that small-scale Langmuir circulations exist. Very recently, Tsai *et al.*[25] performed a DNS of a turbulent liquid flow beneath

a)Author to whom correspondence should be addressed. Electronic mail: kurose@mech.kyoto-u.ac.jp

nonbreaking gravity-capillary waves in which simplified driving shear stress and surface-normal pressure on the liquid surface are given, that is, the coupling between the gas and liquid flows is neglected. They concluded that the scalar transfer across the gas-liquid interface is controlled both by the turbulent eddies and the Langmuir circulations. However, each contribution of turbulent eddies and Langmuir circulations on the liquid-side scalar transfer coefficient has not been fully clarified yet.

The purpose of this study is therefore to investigate the effects of turbulent eddies and Langmuir circulations on scalar transfer across a sheared wind-driven gas-liquid interface by a DNS of a gas–liquid two-phase turbulent flow with a wind-driven nonbreaking wavy interface. In order to exactly evaluate the relationship between the turbulent eddies and Langmuir circulations and their effects on the scalar transfer in realistic wind-driven turbulence, the development of the wind waves from a stationary state is strictly simulated by coupling the gas and liquid flows, as in Komori *et al.*[17]

II. NUMERICAL SIMULATION

The wind-driven wavy gas-liquid interface was captured using an arbitrary Lagrangian-Eulerian (ALE) method with boundary-fitted coordinates (BFC) on moving grids (Komori *et al.*;[17,26] Fulgosi *et al.*;[27] Lin *et al.*[28]). The numerical procedure of the DNS used here was the same as in Komori *et al.*[17] but to capture the Langmuir circulations, the computational domain was set to be larger than that in Komori *et al.*[17]

The non-dimensional governing equations for an incompressible Newtonian fluid flow with scalar transfer are given by the equation of continuity, Navier-Stokes (N-S) equation, and transport equation of passive scalar using the Einstein summation convention

$$\frac{\partial U_i}{\partial x_i} = 0, \tag{1}$$

$$\frac{\partial U_i}{\partial t} + U_j \frac{\partial U_i}{\partial x_j} = -\frac{\partial p}{\partial x_i} + \frac{1}{Re} \frac{\partial^2 U_i}{\partial x_j \partial x_j} + \frac{1}{Fr} \delta_{i3}, \tag{2}$$

$$\frac{\partial C}{\partial t} + U_j \frac{\partial C}{\partial x_j} = \frac{1}{Re \cdot Sc} \frac{\partial^2 C}{\partial x_j \partial x_j}, \tag{3}$$

where U_i is the ith component of the velocity vector ($i = 1, 2$, and 3 denote the streamwise, spanwise, and vertical directions, respectively), p the pressure, δ_ij the Kronecker's delta, and C the passive scalar. The non-dimensional parameters, Re, Sc, and Fr are defined as

$$Re = \frac{U_0 L_0}{\nu}, \; Sc = \frac{\nu}{D}, \; Fr = \frac{U_0^2}{g L_0}, \tag{4}$$

where L_0 and U_0 are the reference length and velocity, ν is the kinematic viscosity, D the molecular diffusivity of scalar, and g the acceleration of gravity. On the gas-liquid interface, two boundary conditions should be satisfied. One is the kinematic boundary condition that describes the Lagrangian behavior of the fluid particle on the free surface, and the other is the dynamic boundary condition which is determined from the balance of stresses acting on the interface in the normal and tangential directions.

The computational domain and numerical grids for the computations of flows in the gas and liquid are shown in Figure 1. The size of the computational domain was $6\delta \times 4.2\delta \times 3\delta$ in the streamwise (x), spanwise (y), and vertical (z) directions. The origin ($x = y = z = 0$) was located at the height of 2δ from the bottom, and the initial flat gas-liquid interface which divides the two-phase flow between upper gas and lower liquid streams was placed on the plane of $z = 0$. The grid points used in the streamwise (x), spanwise (y), and vertical (z) directions were $300 \times 210 \times 90$ on the gas side and $300 \times 210 \times 180$ on the liquid side, respectively. The grid spacing was equidistant in the streamwise (x) and spanwise (y) directions, and to get high resolution, the nonuniform meshes clustered in the gas-liquid-interface region were used in the vertical (z) direction. Periodic boundary conditions were applied in the streamwise (x) and spanwise (y) directions, and the slip boundary condition was applied at the top and bottom boundaries. For the initial conditions of flow field, a

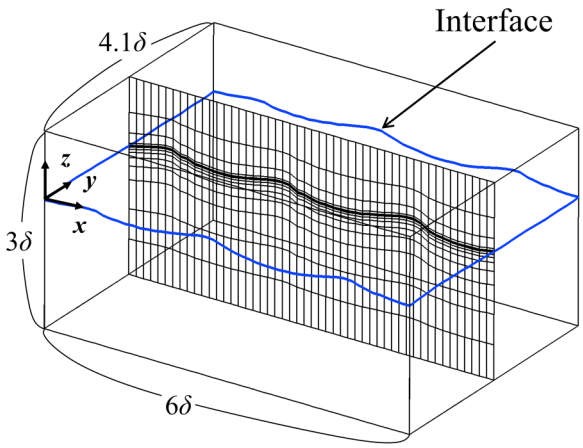

FIG. 1. Computational domain and grids depicted coarsely. The arrow shows an instantaneous location of the gas-liquid interface.

fully developed wall turbulent flow and a quiescent flow were imposed on the gas and liquid sides of the initial flat interface, respectively. For the computation of scalar transfer on the liquid side, the boundary conditions for the passive scalar at the gas-liquid interface and the bottom boundary were given by $C = 1.0$ and Neumann condition, respectively. The marker and cell (MAC) method (Harlow and Welch[29]) was used to solve the Navier-Stokes equation. In order to induce a realistic deformation at the gas-liquid interface, a fully developed wall turbulence for an initial uniform velocity of $U_{\infty,\mathrm{ini}} = 5.8$ m/s and an initial friction velocity of $u_{*,\mathrm{ini}} = 0.24$ m/s were given on the gas side over a flat quiescent liquid. The gas flow was driven by a pressure gradient imposed in the streamwise direction. The value of the Reynolds number based on $U_{\infty,\mathrm{ini}}$ and height of the computational domain on the gas side ($\delta = 2.5 \times 10^{-2}$ m), Re_{ini}, was 9670 and Re_{ini} based on $u_{*,\mathrm{ini}}$ and δ was 400. Also, the values of two non-dimensional times, one based on $U_{\infty,\mathrm{ini}}$ and δ and the other on $u_{*,\mathrm{ini}}$ and δ, were 232 and 9.6, respectively. The density ratio of the gas and liquid was 830, which corresponds to the value for the air-water two-phase flow at about 20 °C. The liquid-side Schmidt number Sc ($= \nu_L/D_L$, where ν_L and D_L are the kinematic viscosity and molecular diffusivity of liquid, respectively) was 1.0. The central processing unit (CPU) time was about 19 200 h for 4 800 000 steps (12 s) on the super computer NEC:SX-9.

III. RESULTS AND DISCUSSION

A. Velocity field

Figure 2 shows the instantaneous configuration of the gas-liquid interface at $t = 6.0$ and 12.0 s. Wind waves were seen to develop and evolve micro-breaking waves (i.e., ripples) on the leeward side of the wind waves. The same wave shape was observed in our previous experiment and prediction and the details are described in Komori *et al.*[17] The conditions of gas flow and wind waves are listed in Table I. Here, the uniform velocity, U_∞, was defined as the velocity on the upper wall of the computational domain. Wind speeds at 10-m height above sea surface, U_{10}, were estimated using the logarithmic profile

$$U_{10} - U_{SURF} = \frac{u_a*}{\kappa} \ln \frac{10}{z_0}, \tag{5}$$

where U_{SURF} is the surface current, κ the von Karman constant, and z_0 roughness length. Here, U_{SURF} is estimated in the same manner as Komori *et al.*[17] Each wind wave was determined by applying the zero-up cross method to the spatial fluctuation of the water level, and the significant wave height, H_S, and significant wave length, L_S, were defined as the mean wave height and length for the largest one-third waves. The phase speed of the significant wind-waves, C_p, was measured by analyzing

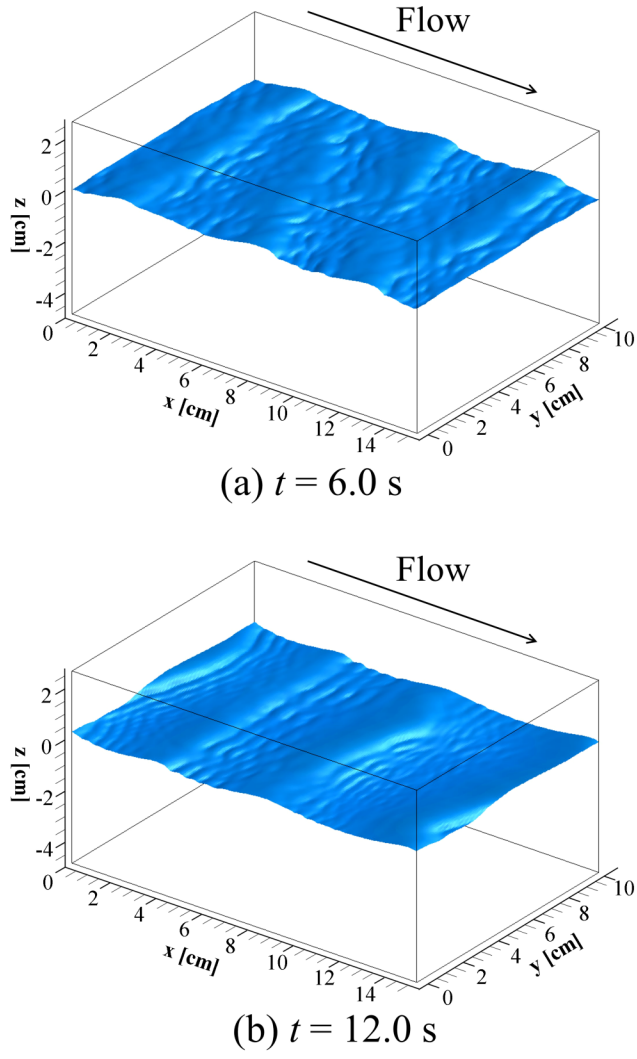

FIG. 2. Instantaneous configuration of predicted gas-liquid interface at (a) t = 6.0 s and (b) t = 12.0 s. Nondimensional lengths based on friction velocity u_w* and liquid-side kinematic viscosity ν_L for x = 1 cm are 100 and 92 at t = 6.0 and 12.0 s, respectively.

the propagation of the significant wind-waves. Although the predicted significant wind-waves were Doppler shifted by the surface current, the statistical properties of the wind-waves were confirmed to be almost consistent with our laboratory data (Takagaki *et al.*[30]) and the dispersed relation for the capitally gravity wave and Toba's 3/2 law (Toba[31]).

TABLE I. Predicted characteristics of gas flow, wind waves, and Langmuir circulations. t: elapsed time, U_∞: free stream wind speed, u_a^*: gas-side friction velocity, U_{10}: wind speed at 10-m height, U_{SURF}: surface current, H_S: significant wave height, L_S: significant wave length, C_P: phase speed of significant wind waves, $D_{Langmuir}$: spacing of liquid-side downward flow, λ_{LS}: secondary-peak spacing on the probability density function of streak spacing of the scalar flux on the liquid surface (see Fig. 9), La: Langmuir number, k: normalized transverse wavenumber of Langmuir circulations based on the spacing between the downward flows.

t (s)	U_∞ (m/s)	u_a^* (m/s)	U_{10} (m/s)	U_{SURF} (m/s)	H_S (m)	L_S (m)	C_P (m/s)	$D_{Langmuir}$ (m)	λ_{LS} (m)	La (–)	k (–)
6.0	4.30	0.277	8.59	0.081 3	0.002 47	0.036 5	0.325	0.029 2	...	0.003 25	1.25
12.0	3.48	0.256	7.42	0.073 7	0.003 86	0.050 1	0.351	0.046 8	0.040 6	0.005 87	1.07

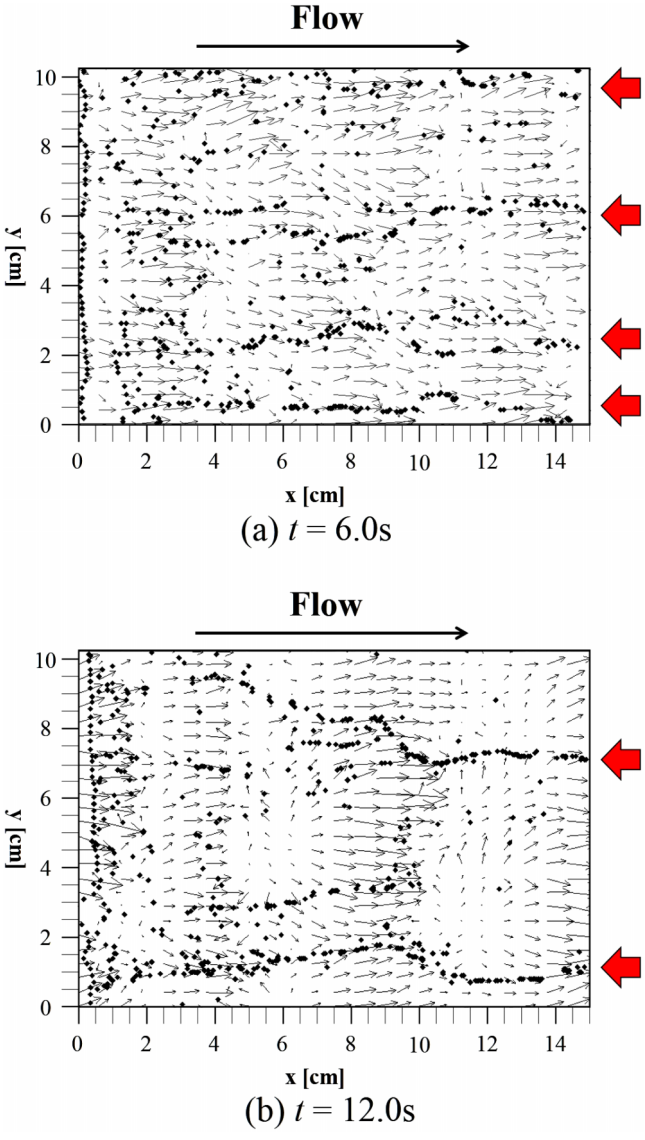

FIG. 3. Instantaneous distributions of marker particles (bold circles) and velocity vectors on the gas-liquid interface at (a) t = 6.0 s and (b) t = 12.0 s. Arrows show streak locations. Nondimensional lengths are as given in Fig. 2.

Figure 3 shows the instantaneous distributions of marker particles and velocity vectors on the gas-liquid interface at t = 6.0 and 12.0 s. Here, the marker particles are initially aligned in the spanwise direction at equal distances along the line x = 0 m and z = 0 m and tracked along the interface without imposing the periodic boundary conditions. The marker particles tended to form fewer streaks with time, and arrows added on the figure clearly indicate the locations of the streaks.

The streaks of the marker particles are considered to be caused by the streamwise vortices, namely, turbulent eddies and/or Langmuir circulations, generated on the liquid side below the wind-driven gas-liquid interface (Komori *et al.*;[9,17] Tsai *et al.*[25]). In order to investigate the liquid-side turbulent structure, we visualized the vortical structure using instantaneous iso-surface of the second invariant Q defined as

$$Q = \frac{1}{2}\left\{\left(\frac{\partial u_i}{\partial x_i}\right)^2 - \frac{\partial u_i}{\partial x_j}\frac{\partial u_j}{\partial x_i}\right\}, \tag{6}$$

where u_i is the ith component of the velocity vector. A positive Q ($Q > 0$) means the presence of vortices and higher Q corresponds to stronger vortices. Figure 4 shows the instantaneous iso-surfaces with high positive values of Q at $t = 6.0$ and 12.0 s, where the iso-surfaces on the liquid side are inscribed in the bottom view. The typical horseshoe vortices associated with bursting motions which are similar to those over the flat rigid wall are observable. In addition, these typical horseshoe vortices locally concentrate and shape streamwise lines in the same locations as

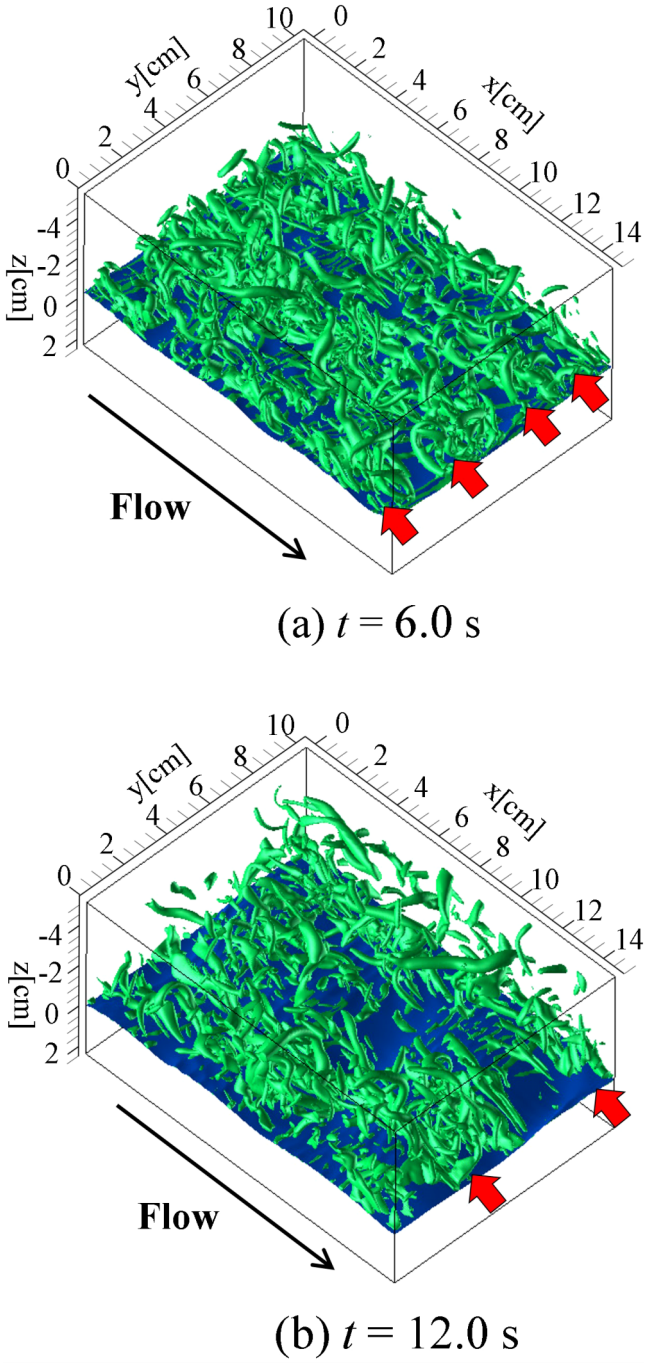

FIG. 4. Instantaneous iso-surfaces of second invariant on the liquid side at (a) $t = 6.0$ s and (b) $t = 12.0$ s (the value of iso-surface is 128 s^{-2}). Arrows show streak locations. Nondimensional lengths are as given in Fig. 2.

surface streaks made by marker particles (see Figure 3). This suggests that there possibly exists a certain fluid motion which forcibly concentrates horseshoe vortices into several streamwise streaks, namely, Langmuir circulations.

Recently, Tsai *et al.*[25] visualized the Langmuir circulations by taking a streamwise-averaging manipulation

$$\dot{\Phi} = \frac{1}{6\delta}\int_0^{6\delta} \Phi dx \tag{7}$$

of the physical variables, Φ, with the turbulent flow fields containing both streamwise vortices and Langmuir circulations to remove the effect of streamwise vortices on the variables. Figure 5

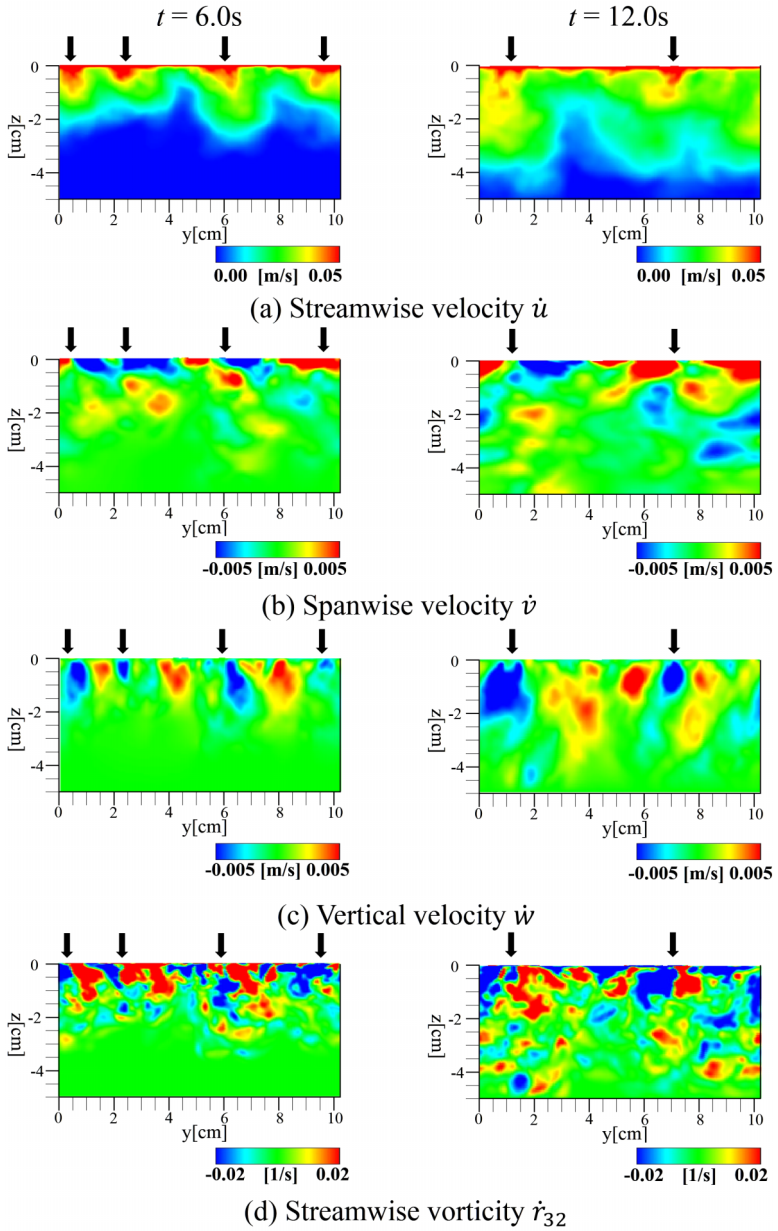

FIG. 5. Cross-sectional (y-z plane) distributions of streamwise-averaged variables on the liquid side at $t = 6.0$ s (left column) and $t = 12.0$ s (right column). Arrows show locations of strong downward flows. Nondimensional lengths are as given in Fig. 2.

shows the cross-sectional (y-z plane) distributions of the streamwise-averaged streamwise velocity $\dot{u}$, spanwise velocity $\dot{v}$, vertical velocity $\dot{w}$, and streamwise vorticity $\dot{r}_{32}$ on the liquid side below the gas-liquid interface at t = 6.0 and 12.0 s. At t = 6.0 s, four solitary parts with strong downstream flow (positive $\dot{u}$) just below the gas-liquid interface can be seen and accompany strong downward flow (negative $\dot{v}$) and pairs of strong vortices (positive and negative $\dot{r}_{32}$) around the strong downstream flow. It was also confirmed that the four solitary parts accompanied fast surface currents. For greater clarification, we added arrows on the strong downward flows. Leibovich[19] and Thorpe[20] pointed out that Langmuir circulations accompanied strong streamwise surface currents and downward flows on the liquid side, and these trends correspond well to the present trends on the predicted liquid flow field (see Figure 5). In addition, the number of pairs of strong vortices is clearly less than that of the instantaneous horseshoe vortices (see Figure 5) and decreases with time (see Figure 5, t = 6.0 and 12.0 s). Therefore, we concluded that the vortices observed in Figures 4 and 5 are turbulent eddies and Langmuir circulations, respectively.

In order to predict whether the Langmuir circulations emerge or not, Leibovich and Paolucci[32] proposed a stability diagram based on the relations between inverse Langmuir number, La^{-1}, and normalized transverse wavenumber based on the spacing between the downward flows (see Figure 5(c)), k. These definitions are as follows:

$$La = \left(\frac{4 {\nu_{L,t}}^3 {k_S}^2}{\sigma H_S^2 u_L^{*2}} \right)^{1/2}, \tag{8}$$

$$k = \frac{k_{Langmuir}}{k_S}, \tag{9}$$

where $\nu_{L,t}$ is the eddy viscosity, $k_S (= 2\pi/L_S)$ the wavenumber of significant wind-waves, σ the significant radian frequency of wind waves, H_S the significant wave height, u_L^* the liquid-side frictional velocity, and $k_{Langmuir}$ $(= 2\pi/L_{Langmuir})$ the dimensional wavenumber based on the spacing between downward flows (see Figure 5(c)). Here, $\nu_{L,t}$ is estimated in the same manner as Tsai *et al.*[25] The value of σ is estimated assuming deep-sea waves, that is, $\sigma = 2\pi C_p/L_S$. According to these definitions, the values for La^{-1} are 307 and 170, and for k are 1.25 and 1.07 at t = 6.0 and 12.0 s, respectively. The values of La and k are listed in Table I. This certainly supports the appearance of the Langmuir circulations in this stability diagram from present and previous studies (Melville *et al.*;[24] Tsai *et al.*;[25] Schnieders *et al.*[33]) (see Figure 6).

B. Scalar concentration field

It is also suggested that these turbulent eddies and/or Langmuir circulations control the scalar transfer across the wind-driven gas-liquid interface (Komori *et al.*;[9,17] Tsai *et al.*[25]). In Figure 7, the

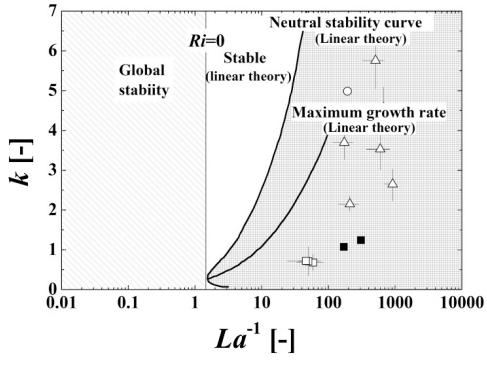

FIG. 6. Neutral stability theory by Leibovich and Paolucci[32] with previous experimental data; ■, present; ○, Tsai *et al.*;[25] □, Melville *et al.*;[24] △, Schnieders *et al.*[33]

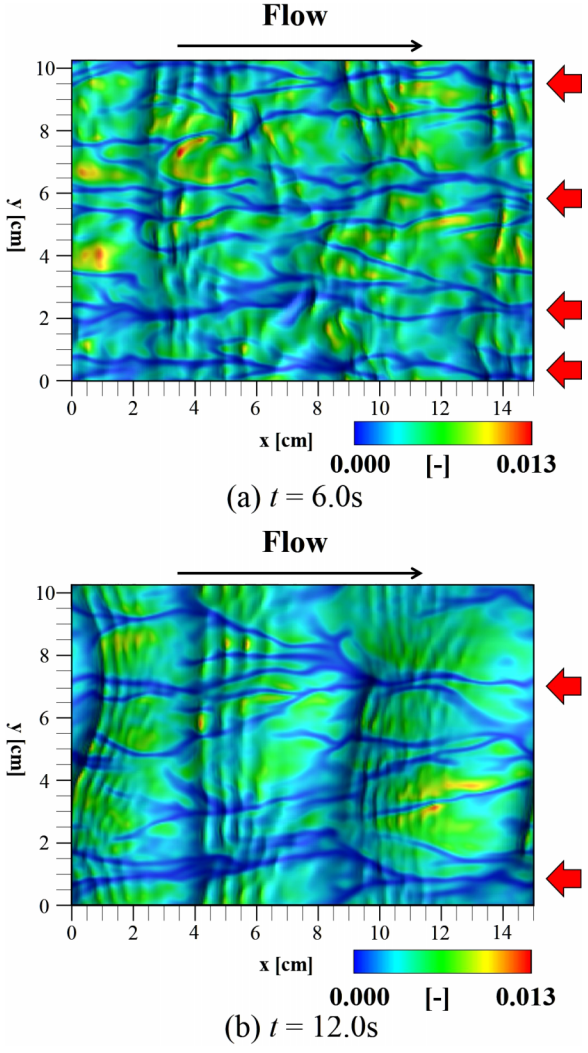

FIG. 7. Distributions of instantaneous scalar flux at (a) t = 6.0 s and (b) t = 12.0 s. Scalar flux is nondimensionalized by friction velocity u_a^* and initial scalar concentration at interface C_i. Arrows show streak locations. Nondimensional lengths are as given in Fig. 2.

distributions of the instantaneous local scalar flux on the gas-liquid interface, F_{local}, at t = 6.0 and 12.0 s are shown. Here, the local scalar flux on the gas-liquid interface is defined as

$$F_{local} = D_L \frac{\partial C}{\partial n}. \tag{10}$$

In addition, Figure 8 shows the cross-sectional (y-z plane) distributions of the instantaneous scalar concentration on the liquid side below the gas-liquid interface at t = 6.0 and 12.0 s. The streaky motions of the scalar flux on the gas-liquid interface are observed to be strongly associated with the streamwise vortices related to downward bursting motions appearing beneath the interface. The scalar transfer mechanism across the wind-driven wavy interface is illustrated in Komori *et al.*[17] (Figure 24). In summary, a pair of streamwise vortices causes downward bursting motions beneath the streaky regions with both low-scalar flux and high streamwise velocity of the gas–liquid interface, and the so-called "happening-of-peeling" process occurs between the downward bursting motions. Due to this process, the surface layer thickness is reduced, and the gradient of scalar concentration increases and the scalar flux is enhanced. When we see the time changes of the instantaneous local scalar flux on the gas-liquid interface and the instantaneous scalar concentration

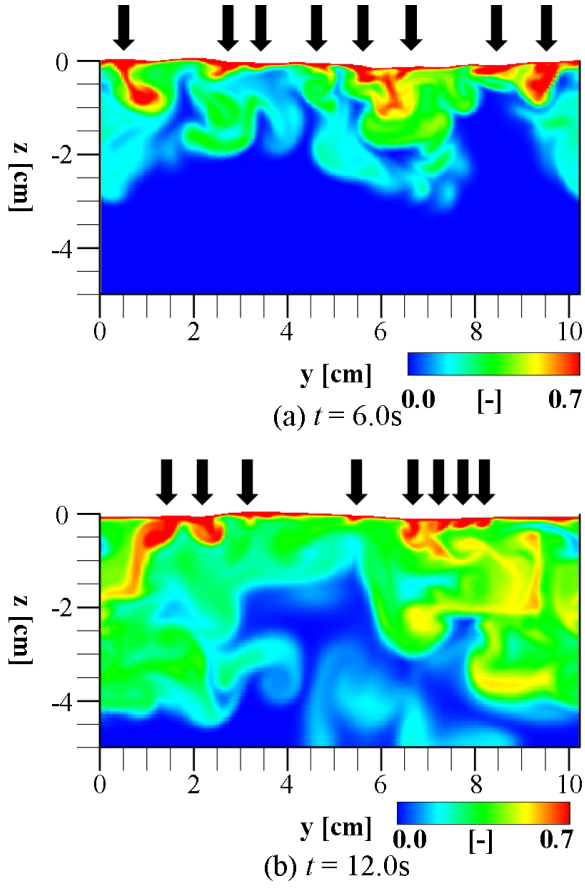

FIG. 8. Cross-sectional (y-z plane) distributions of instantaneous scalar concentration at $x = 3\delta$ on the liquid side at (a) $t = 6.0$ s and (b) $t = 12.0$ s. Scalar concentration is nondimensionalized by initial scalar concentration at interface C_i. Arrows show locations of strong downward flows. Nondimensional lengths are as given in Fig. 2.

on the liquid side in Figures 7 and 8, there seems to be high concentration regions undergoing peeling at $t = 12.0$ s rather than at $t = 6.0$ s.

To investigate the reason why such regions concentrate, we quantitatively evaluated the spacing between low-scalar flux streaks on the gas-liquid interface, λ_{ST}, in Figure 7. Figure 9 shows the probability density functions of the normalized spacing between low-scalar flux streaks, λ_{ST}^+, at $t = 6.0$ and 12.0 s, where λ_{ST} is normalized by the friction velocity on the liquid side u_L^* and kinematic viscosity on the liquid side ν_L. The spacing between low-scalar flux streaks, λ_{ST}^+, almost takes the values ranging from 100 to 200. Generally, the low-speed wall turbulence streaks develop on the wall, and the spacing between low-speed streaks is known to be about 100 (see Smith and Metzler[34]). Considering this presently predicted spacing between low-scalar flux streaks, the streaky structure for the low-scalar flux regions on the gas-liquid interface is induced by the streamwise vortices developing below the gas-liquid interface. Moreover, the spacing between low-scalar flux streaks, λ_{ST}^+, is also found to have values in the region around 400 in the later period at $t = 12.0$ s, which is considered to be attributed to the Langmuir circulations. Then, we compared presently predicted and previously measured spacing of the Langmuir circulations. The present spacing of the liquid-side downward flow $D_{Langmuir}$ (see Figure 7) and secondary-peak spacing λ_{LS} evaluated from Figure 9 are listed in Table I. From the table, it is found that $D_{Langmuir}$ is almost same as λ_{LS} at $t = 12.0$ s, that is, this spacing is really caused by Langmuir circulations. On the other hand, λ_{LS} at $t = 6.0$ s cannot be estimated here because of the difficulty of separation of λ_{LS} from the probability density function of λ_{ST} (see Figure 9). The previously measured spacing λ_{LS}^+ normalized by the

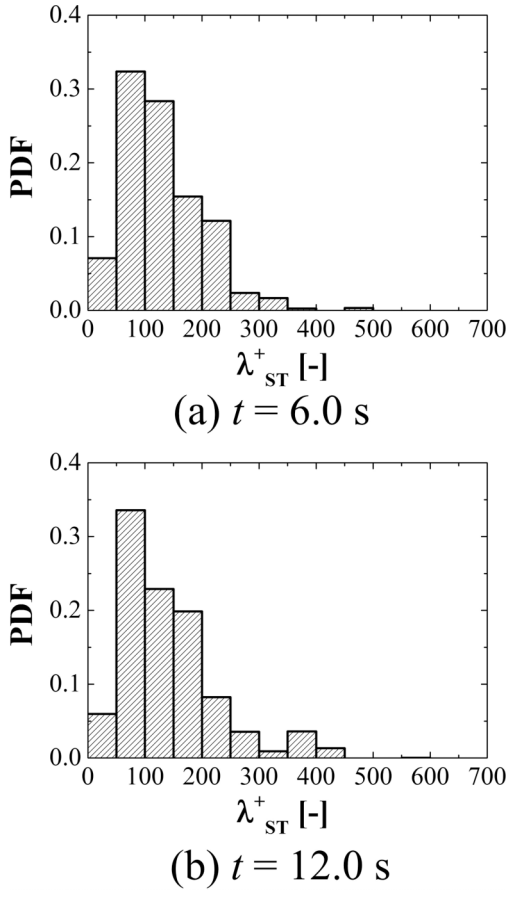

FIG. 9. Probability density function of spacing between low-scalar flux streaks on the interface at (a) $t = 6.0$ s and (b) $t = 12.0$ s.

liquid-side friction velocity u_w^* and liquid-side viscosity (Melville *et al.*,[24] Table I) ranged with 260–290 at $u_a^* = 0.1$–0.22 m/s, using the empirical relation (Komori *et al.*[8])

$$u_a^* = 0.02 U_\infty^{1.5}, \tag{11}$$

and the relation

$$\tau = \rho_a u_a^{*2} = \rho_w u_w^{*2}. \tag{12}$$

The previously measured λ_{LS}^+ (Melville *et al.*[24]) are larger than the spacing between low-speed streaks known to be about 100 (Smith and Metzler[34]), and this trend is similar to the presently predicted λ_{LS}^+ of 375 at $u_a^* = 0.25$ m/s.

It is uncertain as to how the turbulent eddies and/or Langmuir circulations affect the gas-liquid scalar transfer. Then, we applied the streamwise-averaging technique (Eq. (7)) to the scalar concentration on the liquid side to visualize the Langmuir circulations. Figure 10 shows the cross-sectional (y-z plane) distributions of the streamwise-averaged scalar concentration on the liquid side below the gas-liquid interface at $t = 6.0$ and 12.0 s. Pairs of the streamwise-averaged vortices shown by velocity vectors can be seen, with the number of the streamwise-averaged vortices being less than that of the instantaneous vortices (see Figure 8) and decreasing with time. The trend in the numbers of vortices in the scalar concentration field is the same as those for the flow field. This suggests that the vortices observed in Figures 8 and 10 are turbulent eddies and Langmuir circulations, respectively.

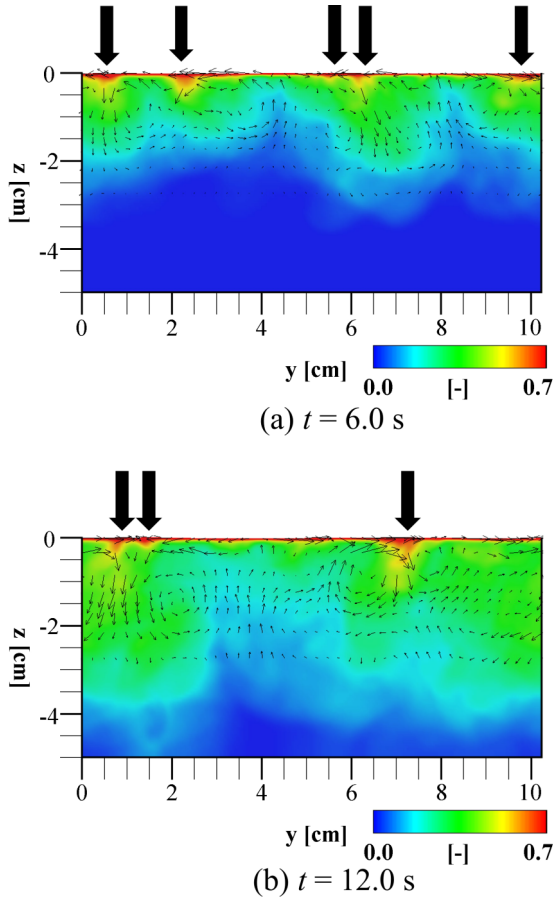

FIG. 10. Cross-sectional (y-z plane) distributions of streamwise-averaged scalar concentration together with velocity vectors on the liquid side at (a) t = 6.0 s and (b) t = 12.0 s. Scalar concentration is nondimensionalized by scalar concentration at interface C_i. Nondimensional lengths are as given in Fig. 2.

C. Scalar transfer coefficient

Figure 11 shows the time series of the scalar coefficient k_L calculated by

$$k_L = \frac{F}{\Delta C} = \frac{1}{(C_i - C_b)} \frac{1}{A} \int_{\text{interface}} D_L \frac{\partial C}{\partial n} dS, \tag{13}$$

where F is the scalar flux at the gas-liquid interface per unit area, ΔC the scalar concentration difference between the interface and bulk liquid, i.e., $\Delta C = C_i - C_b$ (here, C_i and C_b are the scalar concentrations of the interface and bulk liquid, respectively, and C_b is set to be zero in this study), n the normal direction with respect to the gas-liquid interface, A the surface area of the interface, and D_L the molecular diffusivity of scalar on the liquid side. The values of k_L at t = 6.0 and 12.0 s are also listed in Table II.

From Table II and Figure 11, the value of k_L is not found to vary with time between t = 6.0 and 12.0 s regardless of the change in the characteristics of the Langmuir circulations. This suggests that the turbulent eddies in the form of streamwise vortices generated on the liquid side beneath the interface mainly control the scalar transfer across the sheared wind-driven gas-liquid interface, and that the Langmuir circulations act to modulate the turbulent eddies' distribution but barely affect the value of the scalar transfer coefficient k_L. Then, to quantitatively investigate the effect of Langmuir circulations on gas-liquid scalar transfer, we made a rough estimate of the ratio of the scalar transfer coefficient related to the Langmuir circulations to the total scalar transfer coefficient. The gas-liquid

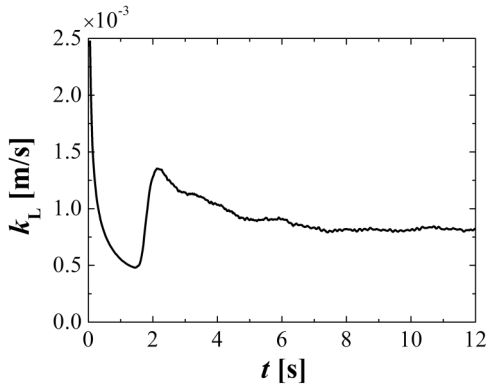

FIG. 11. Time series of scalar coefficient k_{L}.

scalar flux F can be written as

$$F = k_L(C_i - C_b) \sim -\overline{wc} \tag{14}$$

by the bulk model (second equation), and is almost equal to the covariance of the vertical velocity w and scalar concentration c (third equation) near the gas-liquid interface under the assumption that the molecular diffusion term is negligibly small compared with the total scalar flux. By decomposing the vertical velocity and scalar concentration as $w = w_{\mathrm{LC}} + w_{\mathrm{T}}$ and $c = c_{\mathrm{LC}} + c_{\mathrm{T}}$, the equation is rewritten as

$$F \sim -\overline{w_{LC}c_{LC}} - \overline{w_T c_T}, \tag{15}$$

where the subscripts LC and T refer to "Langmuir circulations" and "turbulent eddies" contributions, respectively. Therefore, the first and second terms on the right-hand-side of Eq. (15) are the scalar fluxes due to Langmuir circulations and turbulent eddies, respectively.

Figure 12 shows the spanwise distributions of the streamwise-averaged vertical velocity and scalar concentration at $z = -2$ mm and $t = 12.0$ s. The vertical point of $z = -2$ mm was chosen here because the half height of the significant wind waves is $H_{\mathrm{S}}/2 = 1.9$ mm. Both the streamwise-averaged vertical velocity and scalar concentration fluctuate spanwise with order of the spacing of the Langmuir circulations of $D_{\mathrm{Langmuir}} = 0.0468$ m, although the spanwise fluctuation of the vertical velocity is not clear because the wave length for the turbulent eddies is smaller than $D_{\mathrm{Langmuir}} = 0.0468$ m. In separating the vertical velocity and scalar concentration into contributions due to Langmuir circulations and turbulent eddies, we employed two decomposition methods (1) the low-pass filter and (2) the empirical mode decomposition (EMD), used in Huang *et al.*[35] and Tsai *et al.*[25] The solid (black) curve in Figure 12(a) shows the original vertical velocity. The dashed (red) curve shows the vertical velocity w_{LP} low-pass filtered with the threshold wave-number same as that of the Langmuir circulations ($k_{\mathrm{Langmuir}} = 134$ m^{-1}). The dotted (blue) and dashed-dotted (green) curves show the vertical velocities $w_{\mathrm{EMD,m}}$ calculated by the intrinsic mode functions IMF_{i}

TABLE II. Scalar transfer coefficient and surface divergence. t: elapsed time, U_∞: free stream wind speed, k_{L600}: liquid-side scalar transfer coefficient, β_{RMS1}, β_{RMS2}, β_{RMS3}: root-mean-square value of surface divergence with $VS = 0.5$, 1.0, and 1.5 mm.

t (s)	U_∞ (m/s)	k_{L600} (10^{-5}) (m/s)	β_{RMS1} (s^{-1})	β_{RMS2} (s^{-1})	β_{RMS3} (s^{-1})
6.0	4.30	3.68	42.2	36.5	33.4
12.0	3.48	3.36	40.4	33.6	31.2

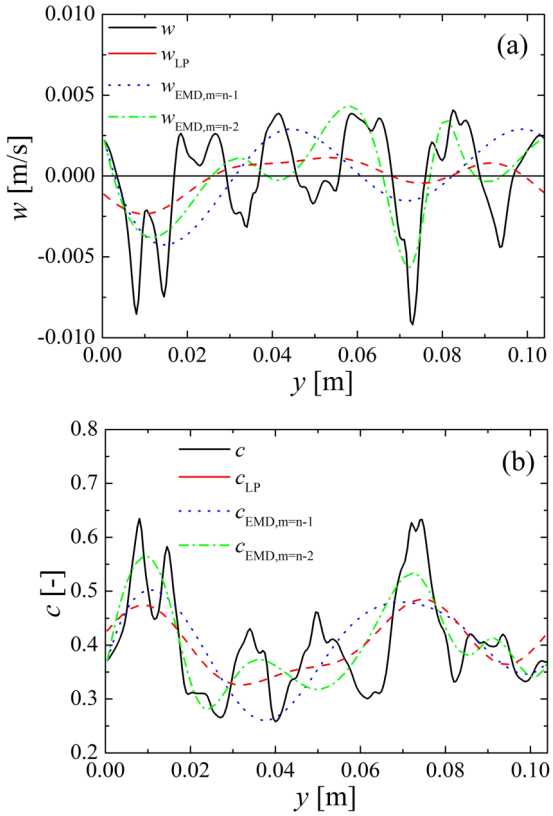

FIG. 12. Spanwise distributions of (a) streamwise-averaged vertical velocity and (b) scalar concentration at $z = -2$ mm and $t = 12.0$ s. Dashed (red) curves show w and c low-pass filtered with a threshold wave-number which is the same as that of the Langmuir circulations ($k_{\mathrm{Langmuir}} = 134\ \mathrm{m}^{-1}$), dotted (blue) and dashed-dotted (green) curves show w and c calculated by the empirical mode decomposition with m = n − 1 and m = n − 2, respectively.

and the residue r_{n} in the EMD algorithm shown as

$$w_{EMD,m} \sim \sum_{i=m}^{n} IMF_i + r_n, \tag{16}$$

where the relations m = n − 1 and m = n − 2 are used to obtain the dotted (blue) and dashed-dotted (green) curves. The curves in Figure 12(b) are the scalar concentrations ($c_{\mathrm{LP}}, c_{\mathrm{EMD,m}}$) calculated in the same manner as in Figure 12(a). We then estimated the three scalar fluxes ($F_{\mathrm{LC1}}, F_{\mathrm{LC2}}, F_{\mathrm{LC3}}$) using the following assumptions:

$$F_{LC1} \sim -\overline{w_{LC1}c_{LC1}} = -\overline{w_{LP}c_{LP}}, \tag{17}$$

$$F_{LC2} \sim -\overline{w_{LC2}c_{LC2}} = -\overline{w_{EMD,n-1}c_{EMD,n-1}}, \tag{18}$$

$$F_{LC3} \sim -\overline{w_{LC3}c_{LC3}} = -\overline{w_{EMD,n-2}c_{EMD,n-2}}, \tag{19}$$

and the scalar fluxes ($F_{\mathrm{T1}}, F_{\mathrm{T2}}, F_{\mathrm{T3}}$) were also estimated as differences between the total scalar flux and each scalar flux F_{LC1}, F_{LC2}, and F_{LC3}, respectively. The ratios $F_{\mathrm{LC1}}/F_{\mathrm{T1}}$, $F_{\mathrm{LC2}}/F_{\mathrm{T2}}$, and $F_{\mathrm{LC2}}/F_{\mathrm{T2}}$ were 2.4%, 12.5%, and 13.2%, respectively. This shows that the effect of the Langmuir circulations on the gas-liquid scalar transfer is relatively small and the gas-liquid scalar transfer is mainly controlled by turbulent eddies near the gas-liquid interface on the liquid side.

Very recently, Sullivan *et al.*[36] reported that the Langmuir circulations are seen not only at low and moderate wind speeds but also at extremely high wind speeds of $U_{10} > 35$ m/s under tropical cyclones. Our results also suggest that such Langmuir circulations under tropical cyclones possibly do not affect the value of the scalar transfer coefficient k_{L} (e.g., McNeil and D'Asaro;[3] Iwano *et al.*[10]) because turbulence becomes large as the wind speed increases.

Presently predicted k_L was compared to previously predicted k_L (Komori *et al.*[17]) and measured k_L (Iwano *et al.*;[10] Turney *et al.*;[37] Krall and Jähne,[38]) normalized using

$$k_L{}^* = \frac{k_{L600}}{u^*}, \tag{20}$$

$$k_L{}^+ = \frac{k_{L600}}{U_\infty}, \tag{21}$$

where U_∞ is the uniform wind velocity and k_L normalized using the assumption (Jähne *et al.*[5])

$$k_{L600} = k_L \left(\frac{Sc_{600}}{Sc} \right)^{-0.5}. \tag{22}$$

Here, Sc is the Schmidt number of the scalar and Sc_{600} is the Schmidt number having the value 600. The previous values of the normalized scalar transfer coefficients were $k_L{}^* = 1.4 \times 10^{-4}$

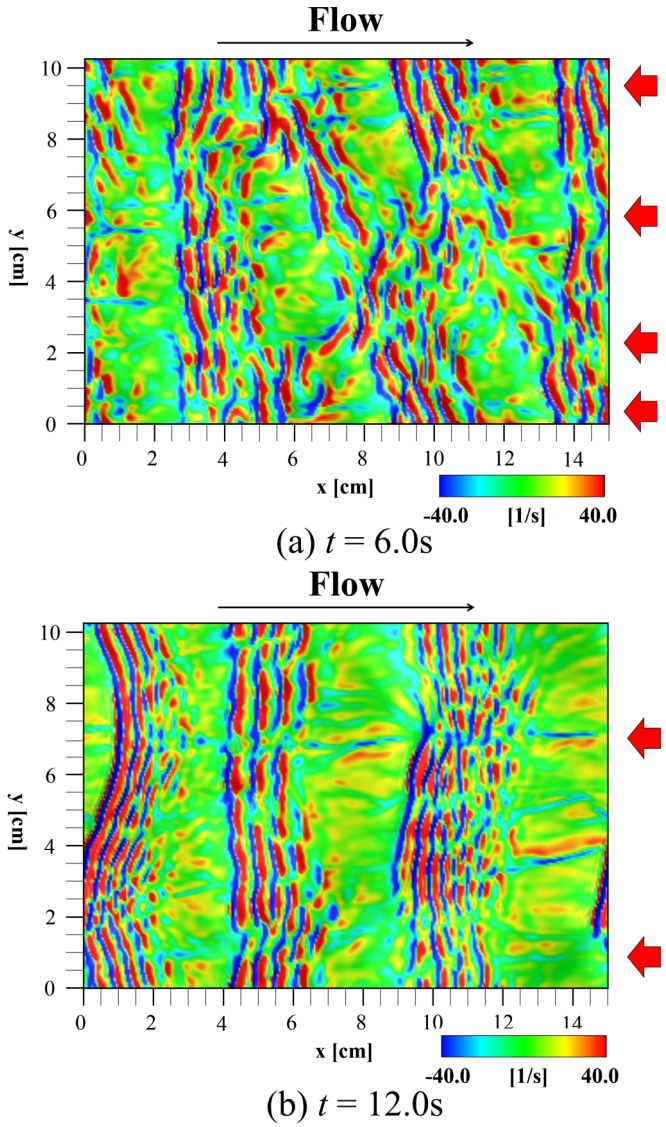

FIG. 13. Distributions of instantaneous surface divergence at (a) $t = 6.0$ s and (b) $t = 12.0$ s. The red and blue areas indicate positive and negative values, that is, the locations where the liquid surface diverges with vertical upward flow and converges with vertical downward flow, respectively. Arrows show streak locations. Nondimensional lengths are as given in Fig. 2.

-2.0×10^{-4} and $k_L{}^+ = 0.6\times10^{-5} - 1.0\times10^{-5}$ within the range of the gas-side friction velocity $u_a{}^* = 0.2$–0.32 m/s. With the present values of $k_L{}^* = 1.3\times10^{-4}$ and $k_L{}^+ = 0.9\times10^{-5}$ at $u_a{}^* \sim 0.27$ m/s, it is clear that k_L almost corresponds to the previously predicted and measured k_L (Komori *et al.*;[17] Iwano *et al.*;[10] Turney *et al.*;[37] Krall and Jähne[38]).

D. Surface divergence model

Since the surface divergence model is one of the suitable models for estimating gas-liquid scalar transfer coefficients (e.g., McCready *et al.*;[39] Banerjee *et al.*[40]), it was used to calculate the surface divergences β

$$\beta = -\left.\frac{\partial w'}{\partial \hat{z}}\right|_{\hat{z}=0} = \left.\left(\frac{\partial u'}{\partial \hat{x}} + \frac{\partial v'}{\partial \hat{y}}\right)\right|_{\hat{z}=0}. \tag{23}$$

Here, $\hat{x}$ and $\hat{y}$ are the tangential directions and $\hat{z}$ is the normal direction. The u' and v' are the tangential fluctuating velocities in the streamwise and spanwise directions and w' is the normal fluctuating velocity. The spacing of the velocity vectors VS is 0.5 mm, as that is the minimum horizontal grid size. Figure 13 shows the distribution of the surface divergence at $t = 6.0$ and 12.0 s. The red and blue areas show positive and negative values, that is, the locations where the divergence/convergence of the liquid surface due to the vertical upward/downward flow occurs. At $t = 6.0$ and 12.0 s, many pairings of areas for divergence and convergence, which are elongated in the spanwise direction, exist at the liquid surface because of capillary waves (so-called ripples) downstream from the wave crests. Moreover, there are streamwise streaks, and the locations of the streaks weakly correspond to that of Langmuir circulations indicated by arrows in Figure 13. To evaluate the surface divergence model for gas-liquid scalar transfer, the root-mean-square values of the surface divergence β_{RMS1} were calculated and are listed in Table II. The values of β_{RMS2} and β_{RMS3} were also calculated with the conditions of velocity-vector spacing $VS = 1.0$ and 1.5 mm, respectively, and are included in Table II, where velocity vectors for spacing $VS = 1.0$ and 1.5 mm were obtained from the original velocity vectors of spacing $VS = 0.5$ mm by box filtering. Figure 14 shows the time series of the RMS values of the surface divergence. The RMS values of the surface divergence take almost constant value between $t = 6.0$ and 12.0 s. Figure 15 shows the relationship between the measured values of the liquid-side scalar transfer coefficient k_L and the values k_{Lmodel} proposed by McCready *et al.*[39] and estimated from the surface divergence model

$$k_{Lmodel} = 0.25\sqrt{\beta_{RMS} D_L}, \tag{24}$$

where D_L is the molecular diffusivity of scalar on the liquid side. We can see good agreement between these measured and estimated values in both present and previous studies (Turney *et al.*[37]).

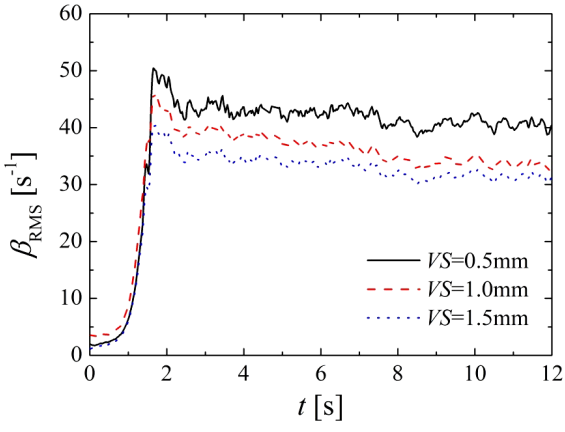

FIG. 14. Time series of RMS values of surface divergence under conditions of velocity-vector spacing $VS = 0.5$, 1.0, and 1.5 mm.

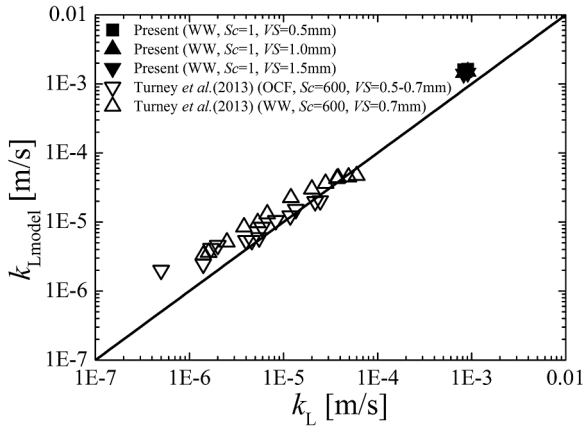

FIG. 15. Relationship between measured and estimated values of the liquid-side scalar transfer coefficient. The values of k_{Lmodel} are estimated using Eq. (24). WW: wind-sheared water surface; OCF: open-channel water surface.

This suggests that surface divergence could be a useful parameter even for instances when Langmuir circulations are present.

IV. CONCLUSIONS

The effects of turbulent eddies and Langmuir circulations in liquid flow on scalar transfer across a sheared wind-driven gas-liquid interface were investigated by means of a DNS of a gas–liquid two-phase turbulent flow with a wind-driven nonbreaking wavy interface. The main results obtained in this study are summarized as follows:

(1) The Langmuir circulations are generated on the liquid side below the sheared wind-driven gas-liquid interface. The trends in the Langmuir circulations accompanying streamwise surface currents and downward flows on the liquid side correspond well to those in previous analytical and experimental studies.
(2) The marker particles on the gas-liquid interface, the turbulent eddies in the form of streamwise vortices on the liquid side (i.e., the typical horseshoe vortices associated with bursting motions), and the low scalar flux lines on the gas-liquid interface induced by the turbulent eddies on the liquid side tend to locally concentrate on the regions along the downward flows caused by the Langmuir circulations.
(3) The cross-sectional (y-z plane) distributions of both the instantaneous and streamwise-averaged scalar concentration on the liquid side below the gas-liquid interface suggest that the turbulent eddies generated on the liquid side beneath the interface mainly control the scalar transfer across the sheared wind-driven gas-liquid interface, whereas the Langmuir circulations act to modulate the turbulent eddies' distribution but hardly affect the value of the liquid-side scalar transfer coefficient. In order to roughly estimate the liquid-side scalar transfer coefficient, the surface divergence could be a useful parameter even in the existence of the Langmuir circulations.

ACKNOWLEDGMENTS

The authors are grateful to Professor Wu-ting Tsai for useful discussion. They also would like to thank Dr. Keigo Matsuda of ESC, JAMSTEC and Mr. Atsushi Kimura for their help in developing the code and data visualization. This research was supported by Ministry of Education, Science, Sports, and Culture Grant-in-Aid (Nos. 24360069 and 25249013). The computations were performed by super computers of Earth Simulator Center, JAMSTEC and National Institute for Environmental Studies, Center for Global Environmental Research.

[1] R. Wanninkhof and W. R. McGillis, "A cubic relationship between air-sea CO_2 exchange and wind speed," Geophys. Res. Lett. **26**, 1889–1892, doi:10.1029/1999GL900363 (1999).
[2] W. R. McGillis, J. B. Edson, J. E. Hare, and C. W. Fairall, "Direct covariance air-sea CO_2 fluxes," J. Geophys. Res. **106**(C8), 16729–16745, doi:10.1029/2000JC000506 (2001).
[3] C. McNeil and E. D'Asaro, "Parameterization of air-sea gas fluxes at extreme wind speeds," J. Mar. Syst. **66**, 110–121 (2007).
[4] B. Jähne, K. O. Münnich, and U. Siegenthaler, "Measurements of gas exchange and momentum transfer in a circular wind-water tunnel," Tellus **31**, 321–329 (1979).
[5] B. Jähne, K. O. Münnich, R. Bösinger, A. Dutzi, W. Huber, and P. Libner, "On the parameters influencing air-water gas exchange," J. Geophys. Res. **92**(C2), 1937–1949, doi:10.1029/jc092ic02p01937 (1987).
[6] B. Jähne, T. Wais, L. Memery, G. Caulliez, L. Merlivat, K. O. Münnich, and M. Coantic, "HE and RN gas exchange experiments in the large wind-wave facility of IMST," J. Geophys. Res. **90**, 11989–11998, doi:10.1029/jc090ic06p11989 (1985).
[7] R. Wanninkhof, "Relationship between wind speed and gas exchange over the ocean," J. Geophys. Res. **97**(C5), 7373–7382, doi:10.1029/92jc00188 (1992).
[8] S. Komori, R. Nagaosa, and Y. Murakami, "Turbulence structure and mass transfer across a sheared air-water interface in wind-driven turbulence," J. Fluid Mech. **249**, 161–183 (1993).
[9] S. Komori, R. Kurose, N. Takagaki, S. Ohtsubo, K. Iwano, K. Handa, and S. Shimada, "Sensible and latent heat transfer across the air-water interface wind-driven turbulence," in *Gas Transfer at Water Surfaces 2010*, edited by S. Komori, W. McGillis, and R. Kurose (Kyoto University Press, Kyoto, 2011), pp. 78–89.
[10] K. Iwano, N. Takagaki, R. Kurose, and S. Komori, "Mass transfer velocity across the breaking air-water interface at extremely high wind speeds," Tellus B **65**, 21341 (2013).
[11] T. Kunugi, S. Satake, and Y. Ose, "Direct numerical simulation of carbon-dioxide gas absorption caused by turbulent free surface flow," Int. J. Heat Fluid Flow **22**, 245–251 (2001).
[12] D. Lakehal, M. Fulgosi, G. Yadigaroglu, and S. Banerjee, "Direct numerical simulation of turbulent heat transfer across a mobile, sheared gas-liquid interface," J. Heat Transfer **125**, 1129–1139 (2003).
[13] D. Lakehal, M. Fulgosi, S. Banerjee, and G. Yadigaroglu, "Turbulence and heat exchange in condensing vapor-liquid flow," Phys. Fluids **20**, 065101 (2008).
[14] D. Lakehal, M. Fulgosi, and G. Yadigaroglu, "Direct numerical simulation of condensing stratified flow," J. Heat Transfer **130**, 021501 (2008).
[15] S. Banerjee, D. Lakehal, and M. Fulgosi, "Surface divergence models for scalar exchange between turbulent streams," Int. J. Multiphase Flow **30**, 963–977 (2004).
[16] S. Banerjee, "Modeling of interphase turbulent transport processes," Ind. Eng. Chem. Res. **46**, 3063–3068 (2007).
[17] S. Komori, R. Kurose, K. Iwano, T. Ukai, and N. Suzuki, "Direct numerical simulation of wind-driven turbulence and scalar transfer at sheared gas-liquid interfaces," J. Turbulence **11**, N32 (2010).
[18] A. D. D. Craik and S. Leibovich, "A rational model for Langmuir circulations," J. Fluid Mech. **73**, 401–426 (1976).
[19] S. Leibovich, "The form and dynamics of Langmuir circulations," Annu. Rev. Fluid Mech. **15**, 391–427 (1983).
[20] S. A. Thorpe, "Langmuir circulation," Annu. Rev. Fluid Mech. **36**, 55–79 (2004).
[21] J. McWilliams, P. Sullivan, and C. Moeng, "Langmuir turbulence in the ocean," J. Fluid Mech. **334**, 1–30 (1997).
[22] P. P. Sullivan and J. C. McWilliams, "Dynamics of winds and currents coupled to surface waves," Annu. Rev. Fluid Mech. **42**, 19–42 (2010).
[23] C. S. Garbe, A. Rutgersson, J. Boutin, B. Delille, C. W. Fairall, N. Gruber, J. Hare, D. Ho, M. Johnson, G. de Leeuw, P. Nightingale, H. Pettersson, J. Piskozub, E. Sahlee, W. Tsai, B. Ward, D. K. Woolf, and C. Zappa, "Transfer across the air-sea interface," *Ocean-Atmosphere Interactions of Gases and Particles*, edited by P. S. Liss and M. T. Johnson (Springer, Berlin, 2014), pp. 55–112.
[24] W. K. Melville, R. Shear, and F. Veron, "Laboratory measurements of the generation and evolution of Langmuir circulations," J. Fluid Mech. **364**, 31–58 (1998).
[25] W. T. Tsai, S. M. Chen, G. H. Lu, and C. S. Garbe, "Characteristics of interfacial signatures on a wind-driven gravity-capillary wave," J. Geophys. Res.: Oceans **118**, 1715–1735, doi:10.1002/jgrc.20145 (2013).
[26] S. Komori, R. Nagaosa, Y. Murakami, S. Chiba, K. Ishii, and K. Kuwahara, "Direct numerical simulation of three-dimensional open-channel flow with zero-shear gas-liquid interface," Phys. Fluids A **5**, 115–125 (1993).
[27] M. Fulgosi, D. Lakehal, S. Banerjee, and V. De Angelis, "Direct numerical simulation of turbulence in a sheared air-water flow with a deformable interface," J. Fluid Mech. **482**, 319–345 (2003).
[28] M.-Y. Lin, C.-H. Moeng, W.-T. Tsai, P. P. Sullivan, and S. E. Belcher, "Direct numerical simulation of wind-wave generation processes," J. Fluid Mech. **616**, 1–30 (2008).
[29] F. H. Harlow and J. E. Welch, "Numerical calculation of time-dependent viscous incompressible flow of fluid with free surface," Phys. Fluids **8**, 2182–2189 (1965).
[30] N. Takagaki, S. Komori, N. Suzuki, K. Iwano, T. Kuramoto, S. Shimada, R. Kurose, and K. Takahashi, "Strong correlation between the drag coefficient and the shape of the wind sea spectrum over a broad range of wind," Geophys. Res. Lett. **39**, L23604, doi:10.1029/2012GL053988 (2012).
[31] Y. Toba, "Local balance in the air-sea boundary processes," J. Oceanogr. Soc. Jpn. **28**, 109–120 (1972).
[32] S. Leibovich and S. Paolucci, "The instability of the ocean to Langmuir circulations," J. Fluid Mech. **102**, 141–167 (1981).
[33] J. Schnieders, S. Garbe, W. L. Peirson, G. B. Smith, and C. J. Zappa, "Analyzing the footprints of near surface aqueous turbulence: An image processing-based approach," J. Geophys. Res.: Oceans **118**, 1272–1286, doi:10.1002/jgrc.20102 (2013).
[34] C. R. Smith and S. P. Metzler, "The characteristics of low speed streaks in the near-wall region," J. Fluid Mech. **129**, 27–54 (1983).
[35] N. E. Huang, Z. Shen, S. R. Long, M. C. Wu, H. H. Shih, Q. Zheng, N. C. Tung, and H. H. Liu, "The empirical mode decomposition and the Hilbert spectrum for nonlinear and non-stationary time series analysis," Proc. R. Soc. London, Ser. A **454**, 903–995 (1998).

[36] P. P. Sullivan, L. Romero, J. McWilliams, and W. K. Melville, "Transient evolution of Langmuir turbulence in ocean boundary layers driven by hurricane winds and waves," J. Phys. Oceanogr. **42**, 1959–1980 (2012).
[37] D. E. Turney and S. Banerjee, "Air-water gas transfer and near-surface motions," J. Fluid Mech. **733**, 588–624 (2013).
[38] K. E. Krall and B. Jähne, "First laboratory study of air–sea gas exchange at hurricane wind speeds," Ocean Sci. **10**, 257–265 (2014).
[39] M. J. McCready, E. Vassilliadou, and T. J. Hanratty, "Computer simulation of turbulent mass transfer at a mobile interface," AIChE J. **32**, 1108–1115 (1986).
[40] S. Banerjee, D. Lakehal, and M. Fulgosi, "Surface divergence models for scalar exchange between turbulent streams," Int. J. Multiphase Flow **30**, 963–977 (2004).